Soft Matter

Accepted Manuscript

This article can be cited before page numbers have been issued, to do this please use: T. Yamamoto and M. Sano, *Soft Matter*, 2017, DOI: 10.1039/C7SM00337D.

ROYAL SOCIETY OF CHEMISTRY

rsc.li/soft-matter-journal

View Article Online
DOI: 10.1039/C7SM00337D
ROYAL SOCIETY OF CHEMISTRY

Journal Name

ARTICLE TYPE

Cite this: DOI: 10.1039/xxxxxxxxxx

Chirality-induced helical self-propulsion of cholesteric liquid crystal droplets†

Takaki Yamamoto*[a] and Masaki Sano*[a]

Received Date
Accepted Date

DOI: 10.1039/xxxxxxxxxx

www.rsc.org/journalname

We report the first experimental realization of a chiral artificial microswimmer exhibiting the helical motion without any external fields. We discovered that a cholesteric liquid crystal (CLC) droplet with a helical director field swims in a helical path driven by the Marangoni flow in an aqueous surfactant solution. We also showed that the handedness of the helical path is reversed when that of the CLC droplet is reversed by replacing the chiral dopant with the enantiomer. In contrast, nematic liquid crystal (NLC) droplets exhibited ballistic motions. These results suggest that the helical motion of the CLC droplets is driven by chiral couplings between the Marangoni flow and rotational motion via helical director field of CLC droplets.

1 Introduction

The role of chirality in microswimmers, which are microscopic objects spontaneously moving in fluids without any external fields, has been receiving increasing attention in the field of biological physics[1–3]. Owing to the biomolecular chirality, chiral motions are remarkable in biological microswimmers; for instance, a sperm of a sea urchin controls its flagellum to steer in circular and helical paths[4–6]. Recently, to study the microswimmers' dynamics without difficulties in controlling biological systems, experimental setups of artificial microswimmers have been established and their dynamics have been intensively investigated[7,8]. Kümmel *et al.* experimentally observed the circular motion of a chiral artificial microswimmer in two dimensions (2D) using an L-shaped self-propelled particle[9]. However, there have been no studies reporting a chirality-induced helical motion of an artificial microswimmer in 3D yet. In this paper, we present the first experimental realization of a chiral artificial microswimmer exhibiting the helical motion.

Self-propulsions of droplets in/on fluid, such as a moving alcohol droplet on water[10], have been intensively investigated[11–13]. The underlying mechanism of the self-propulsion is the Marangoni flow induced by the gradient of the surface tension at the liquid-liquid interface[14]. Recently, Herminghaus *et al.* reported nematic liquid crystal (NLC) droplets can also swim in a surfactant solution[15,16].

A cholesteric liquid crystal (CLC), which shows a helical director field due to the chirality of molecules, undergoes rotational motion when subjected to external fields such as a temperature gradient[17–20]. This rotational motion is explained as a result of the cross coupling between axial (rotational motion) and polar (external field) vectorial quantities only allowed in chiral systems due to symmetry argument[21]. Hence, a CLC droplet in a surfactant solution can swim in a chiral path owing to the chiral coupling between the Marangoni flow and rotational motion.

2 Material and method

In our experiments, a mixture of the NLC (5CB (4-cyano-4'-pentylbiphenyl), TCI) and 2wt% of a chiral dopant (R811, WuXi AppTec Co., Ltd), which works as a CLC, was dispersed in an aqueous surfactant solution (13wt%, TTAB (tetradecyltrimethylammonium bromide[15]), Wako) as described below. To eliminate the effect of the buoyancy on the swimming behavior of the CLC droplets, we adjusted the density of surfactant solutions using a mixture of D_2O and H_2O as a solvent[16]. We measured the density of surfactant solutions with different compositions of D_2O/H_2O using density meter (DMA5000s, Anton Paar, accuracy: $1 \cdot 10^{-5}$ g/cm^3, see also Fig. S1, ESI†). In our experiments, we used D_2O/H_2O with 25wt% D_2O, whose density (1.02233 g/cm^3) is well matched with that of CLC (1.02175 g/cm^3).

As shown in Fig. 1, after pipetting a surfactant solution into a chamber made of a cover glass and a double-sided tape with a hole (diameter: $3 \sim 4$ mm, thickness: ~ 750 μm), CLC droplets were injected into the solution using a microinjector (Femtojet, Eppendorf) with commercially available needles (Femtotips, Eppendorf). Then, the chamber was encapsulated with an upper cover glass. To investigate the 3D dynamics of the CLC droplets, we used spacers much thicker than the diameter $D \approx 20$ μm of CLC droplets we observed. The sizes of the CLC droplets were adjusted by controlling the injection pressure p_i and injection time

[a]Department of Physics, The University of Tokyo, 7-3-1 Hongo, Bunkyo-ku, Tokyo 113-0033, Japan; E-mail: tyamamoto@daisy.phys.s.u-tokyo.ac.jp

† Electronic Supplementary Information (ESI) available: [details of any supplementary information available should be included here]. See DOI: 10.1039/b000000x/

View Article Online
DOI: 10.1039/C7SM00337D

t_i of Femtojet. While the appropriate parameters are different for each needle, this setup enables us to produce microdroplets with a precision of submicron order.

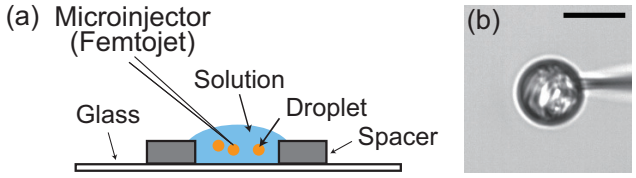

Fig. 1 Production of CLC droplets by Femtojet. (a) The sizes of the droplets were adjusted by controlling the injection pressure p_i and the injection time t_i. (b) An image of an injected droplet ($D_0 = 20.4$ μm) acquired just before the release of the droplet from the tip of Femtotip ($p_i = 1950$ hPa, $t_i = 1.0$ s). The scale bar is 20 μm.

The dynamics of CLC droplets in the surfactant solution were observed with an inverted optical microscope without any polarizers unless otherwise noted (DMI6000B, Leica). The time-lapse images were acquired using a CMOS camera (HXG40, Baumer, 10 frames/sec). While we were manually focusing on each swimming CLC droplet during the acquisition, XY coordinates of the XY stage (TANGO Desktop, Märzhäuser Wetzlar) and Z coordinate of the motorized Z drive of objective lens ($\times$4 or $\times$20, Leica) were recorded through Labview programming. Then, we reconstructed the 3D trajectory of the droplet from the recorded XYZ coordinates and the position of the center of mass of the droplet in each image. Here, after the image was binarized, we specified the region of the droplet and detected the center of mass (See also Fig. S2, ESI†). We conducted our experiments at 25°C.

3 Results

Figure 2 shows the 2D projected trajectories of CLC droplets (initial diameter: $D_0 = 19.3 \sim 20.2$ μm) observed through the low power of the microscope ($\times$4). Here, we fixed the position of XY stage and Z drive. The focal plane of the objective lens was set at the upper cover glass. We injected the droplets ($N = 7$) sequentially within 20 s. The trajectories 2 min after the injection of the first droplet were drawn in Fig. 2. The center of mass of each droplet was tracked until the droplets stop swimming or escape outside the field of view. Some parts of the trajectories are not drawn since the tracking was difficult when the droplets collided or were hindered by obstacles. As a result, we observed zig-zag motions in 2D images for all the droplets which did not escape.

Figure 3(a) and (b) show the 2D and 3D trajectories of a single CLC droplet. Here, we manually focused on the swimming CLC droplet through the high power of the microscope ($\times$20) during the observation. We injected 3 droplets ($D_0 = 20.2 \sim 20.6$ μm) within 20 s and tracked one of them. Since our droplet swam due to the Marangoni flow induced by the dissolution of LC into surfactant solution[15], the size of the droplet decreased during the locomotion. Figure 4 (a) shows the time evolution of diameter of the droplet, where the origin of time is set to the time when the first droplet was injected. We found that the diameter decreased linearly in time (1.2 μm/min). Assuming the constant dissolution rate at the surface of the droplet, such linear damping of the

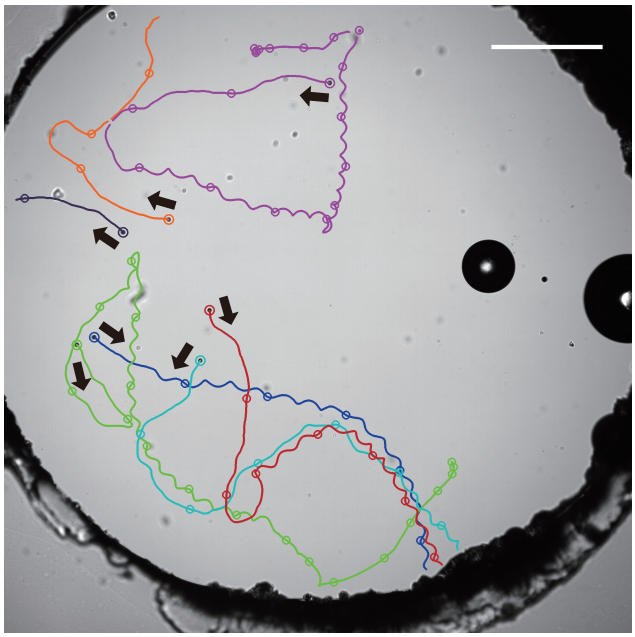

Fig. 2 2D projected trajectories of the CLC droplets injected during a short period (20 s). We drew the trajectories 2 min after the first droplet was injected. The droplets swam in the direction of arrows. The circles on the trajectories are drawn every 30 s. The large dark circles are air bubbles which entered the chamber during the encapsulation. The scale bar is 500 μm.

diameter is derived. Also, the time evolution of z coordinate, absolute value and xyz components of velocity of the droplet are shown in Fig. 4 (b)-(f). Here, we reduced high-frequency noise in the recorded coordinates using Butterworth filter with the cut-off frequency $f_c = 0.5$ Hz before calculating the velocity (See also Figs. S3 and S4, ESI†). We noted that the droplets had a tendency to move upward at the beginning and frequently arrive at the upper glass during the locomotion as shown in Fig. 4(b), even though the effect of the buoyancy was carefully suppressed using D_2O. The bias would be due to the thermal convection which is notoriously inevitable in such thick cells as ours, or flow which occurs on encapsulating the chamber with the top cover glass.

In the single trajectory, the CLC droplet underwent three phases exhibiting different textures and motions. In the first phase "D-phase (Defomation-phase)" from $t = t_{\mathrm{d}}$ to $t = t_{\mathrm{s,i}}$ (Fig. 3(a)), the droplet swam meandering with the deformed director field stirred by the Marangoni flow (Fig. 3 (a-1)). As we will see later, when the director field is not stirred by the Marangoni flow, the CLC droplet does not exhibit such meandering behavior but rather deterministic behavior. Hence, the meandering behavior should be due to the complicated spatiotemporal modulation of the director field.

In the "S-phase (Striped-phase)" from $t = t_{\mathrm{s,i}}$ to $t = t_{\mathrm{s,f}}$, the droplet exhibited a striped pattern (Fig. 3(a-2)) which means the homogeneous helical director field as sketched in Fig. 3 (c). Here, we defined $t_{\mathrm{s,i}}$ when we clearly observed a homogeneous striped pattern. We also observed a spiral pattern in Fig. 5(a-1) during the S-phase, when the helical axis of the droplet is perpendicular to the horizontal plane. Hence, we deduce that the CLC

View Article Online
DOI: 10.1039/C7SM00337D

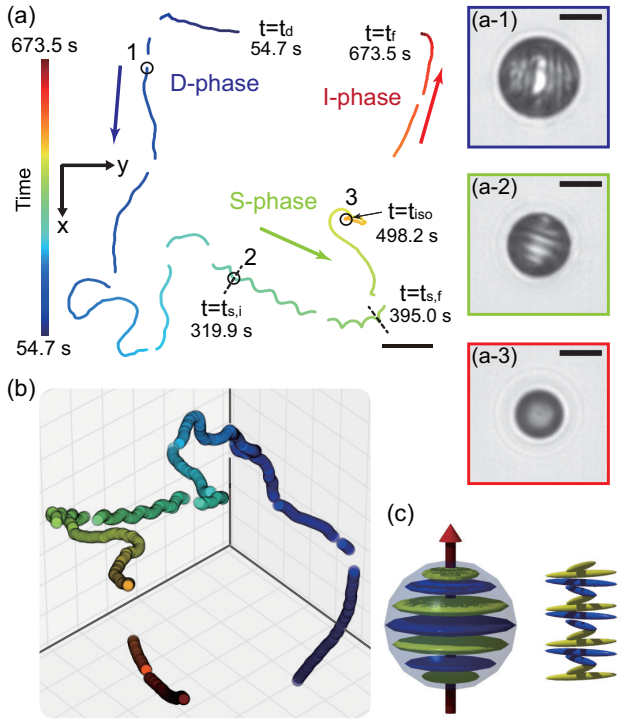

Fig. 3 (a)(b) The 2D and 3D trajectories of a CLC droplet. The gradient of color and the arrows represent the time evolution. The gaps in the trajectory are due to the lack of data during moving the XY stage. (a-1)-(a-3) The textures of the droplets observed at the three points marked with circles in (a), respectively. (c) Schematic image of a droplet with uniform helical director field, corresponding to (a-2). Spheroids represent CLC molecules. The red arrow indicates the helical axis of CLC. The scale bars are 200 μm in (a) and 10 μm in (a-1)-(a-3), respectively.

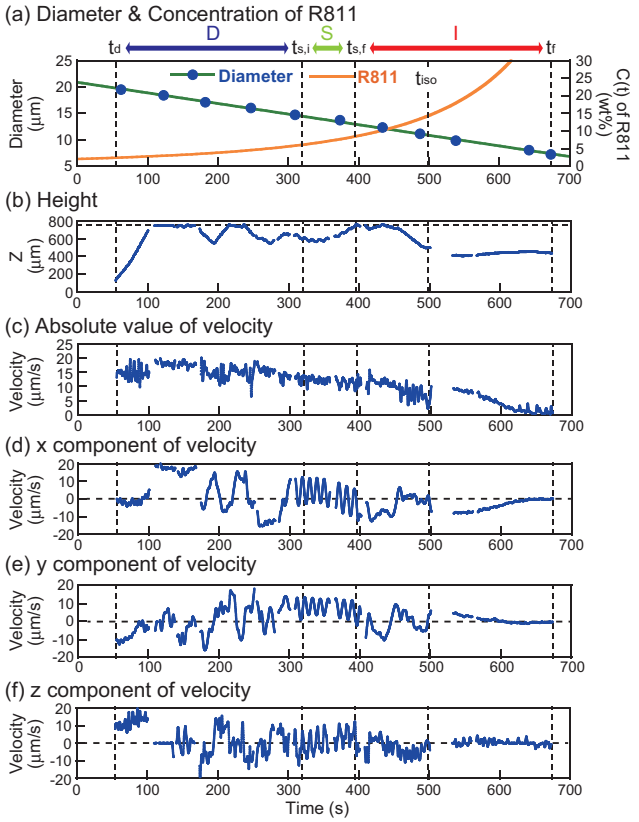

Fig. 4 Time-evolution of (a) diameter and concentration $c(t)$ of R811, (b) height (z coordinate), (c) absolute value of velocity, (d)(e)(f) xyz components of the velocity of the droplet corresponding to Fig. 3. The data for diameter in (a) is fitted with a green line. The vertical lines indicate $t = t_{\rm d}, t_{\rm s,i}, t_{\rm s,f}, t_{\rm iso}, t_{\rm f}$, respectively. In (b), the z coordinate of the bottom glass is set to 0 μm. The dashed line in (b) indicates the height of the upper glass ($z = 755$ μm).

droplet has a spiral disclination loop at the surface, while it has a homogeneous helical director field inside. Such a director field is reported to be realized under homeotropic anchoring conditions[22,23]. As we will see later in Fig. 7(b)-(d), the radial director field observed in the NLC droplets ensures that TTAB aqueous solution provides a homeotropic anchoring condition on the surface of the LC droplets. In the S-phase, we observed a 2D zig-zag motion, which is a helical motion in 3D as we will show below.

In the final phase "I-phase (Isotropic-phase)" from $t = t_{\rm s,f}$ to $t = t_{\rm f}$, the striped pattern of the CLC droplet gradually deformed and then the droplet got isotropic completely at $t = t_{\rm iso}$ (Fig. 3(a-3)). We defined $t_{\rm iso}$ when the deformation of the director field disappeared and the texture of the droplet got isotropic under a microscope without polarizers. We confirmed the isotropy of the CLC using crossed polarizers during the period just after $t = t_{\rm iso}$ in which the trajectory of the droplet is not shown in Fig. 3(a) due to the difficulty in tracking under a microscope with crossed polarizers. The image observed using crossed polarizers is shown in Fig. S5 (ESI†). The ballistic motion of the isotropic CLC droplet observed after $t = t_{\rm iso}$ is consistent with that of the isotropic NLC droplet[15].

Why do the 3 phases exist in a life of the CLC droplet? We consider that the transition from the D-phase to the S-phase is understood by the Ericksen number $Er = \eta v L/K$, a non-dimensional number defined by the ratio of the viscous to elastic force. Here, v, η, L, K are the characteristic velocity, viscosity, length and elastic constant of LC, respectively. Defining the Ericksen number Er for a CLC droplet, the characteristic velocity and length are the velocity v and the diameter D of a CLC droplet. In our experiments, the size and the velocity of the droplet decreased as shown in Fig. 4(a) and (c). Therefore, assuming constant values for K and η, Er decreases as the CLC droplet shrinks. As a result, in the S-phase, the deformation of the director field due to the Marangoni flow is suppressed and the CLC droplet exhibits a homogeneous helical director field without deformation. Using the physical properties $\eta \approx 0.06$ Pa$\cdot$s[24] and $K \approx 7 \cdot 10^{-12}$ N[25], which are average values for 5CB, and typical experimental parameters $D \approx 20$ μm and $v \approx 20$ μm/s, we obtain $Er \approx 3$, which is consistent with our discussion above, since the effect of viscosity and that of elasticity balance when $Er = \mathcal{O}(1)$.

Meanwhile, we consider that the transition from the S-phase to the I-phase is due to the insolubility of chiral dopant R811 in the surfactant solution, which we confirmed by putting a powder of R811 in the solution. Due to the insolubility, the concentration of R811 should increase as the droplet shrinks. Since the cholesteric-isotropic transition temperature $T_{\rm iso}$ decreases as the concentration of R811 increases (see Fig. S6, ESI†), $T_{\rm iso}$ of the

View Article Online
DOI: 10.1039/C7SM00337D

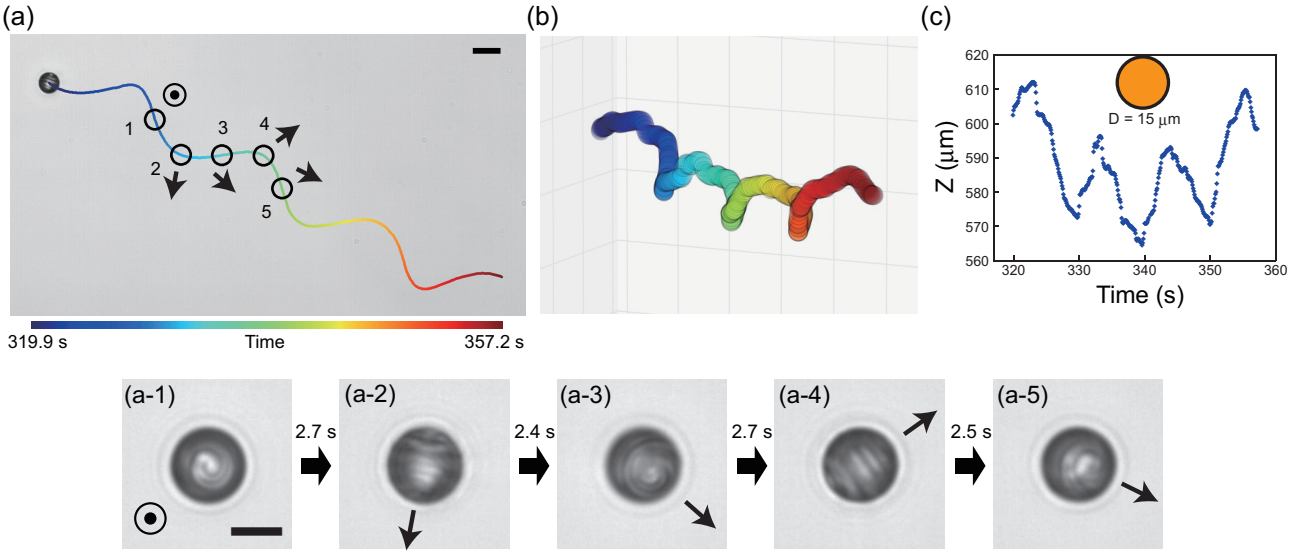

Fig. 5 (a) 2D and (b) 3D trajectory of a R811-doped CLC droplet during the S-phase. The textures of the CLC droplet at the points 1-5 in (a) are shown in (a-1)-(a-5). The arrows in (a) and (a-1)-(a-5) indicate the direction o the helical axis of CLC droplets. (c) Time evolution of the z coordinate of the droplet. We depict the orange circle with the diameter 15 μm as a reference of the size of the CLC droplets. The scale bars in (a) and (a-1) are 20 μm and 10 μm, respectively.

CLC droplet decrease in the shrinking process. In Fig. 4(a), we estimated the concentration $c(t)$ of R811 in the CLC droplet. Here, we used a relation $c(t) = c_0(D_0/D(t))^3$, where c_0 and $D(t)$ denote the initial concentration of R811 (2wt%) and the diameter at time t, respectively. The linear fit to the experimental data of $D(t)$ provided $c(t_{\rm iso}) = 14.2$wt%, at which $T_{\rm iso}$ is 26.4°C (see Fig. S6, ESI†). We thus consider that the CLC droplet got isotropic because $T_{\rm iso}$ of the CLC droplet approached our experimental temperature 25°C.

Figure 5(a) and (b) show a part of the 2D and 3D trajectory during the S-phase in Fig. 3(a). We found that the CLC droplet with homogeneous helical director field swam in a left-handed helical path. Here, a helix is left-handed, if the rotational direction is anti-clockwise. Note that the droplet in Fig. 5 swims in the helical path ≈ 10 times the diameter (≈ 15 μm) of the droplet away from the top glass ($z = 755$ μm). Since the self-propelled droplet exerts no net force on the surrounding fluid, the slowest decaying mode of the velocity field around the droplet, which is characterized by a force dipole (a singularity solution of the Stokes equation), decays as $1/r^2$, where r denotes the distance from the center of the droplet[26]. We thus consider that the hydrodynamic field around the droplet decays enough at the top glass that we can neglect the effect of hydrodynamic interaction between the droplet and the top glass. Consequently, the CLC droplet swims in the helical path as a true 3D character. In Fig. 5(a-1)-(a-5), the time-evolution of the texture of the CLC droplet and the direction of the helical axis of the droplet during the helical motion are shown. We found that the helical axis of the droplet precesses around the helical axis of the helical path, which we call "precession of helical axis" in this paper. This observation means that the helical director field of the droplet and the helical motion couple. Importantly, all the CLC droplets we tracked showed left-handed helical paths and precession of helical axis ($N = 4, D_0 = 20.0 \sim 20.8$ μm). The handedness, radius r, pitch P, period T and absolute value v of velocity of the helical motion are summarized in Table 1. We measured these parameters from the 2 periods of the helical trajectories when the droplets have a same diameter (14.5 μm).

To confirm that the helicity of the helical path is determined by the chirality of CLC, we tracked the swimming CLC droplets doped with a chiral dopant S811 (2wt%), which is the enantiomer of R811. A typical 2D trajectory of a S811-doped droplet is shown in Fig. 6(a). As observed in the case of the R811-doped droplets, the S811-doped droplet underwent the D-, S- and I-phases. However, as shown in Fig. 6(b), we found that the S811-doped droplet swam in a right-handed helical path during the S-phase, while the helix parameters were similar to those of the R811-doped droplets swimming in left-handed helical paths (Table 1, $N = 4, D_0 = 19.7 \sim 21.7$ μm). Precession of helical axis was also observed for the S811-doped droplets.

Table 1 The helix parameters of the helical motion of the CLC droplets doped with either R811 or S811 ($N = 4$, respectively). The handedness of helical path is abbreviated as H.

Dopant	H	r (μm)	P (μm)	T (s)	v (μm/s)
R811	Left	14.3 ± 3.1	108.2 ± 15.2	10.6 ± 0.7	12.9 ± 2.0
S811	Right	13.8 ± 1.3	108.1 ± 6.7	10.5 ± 0.2	12.7 ± 2.3

In contrast, we observed only ballistic motion for NLC droplets (only 5CB) when the diameters are below 20 μm. In Fig. 7(a), we show the 2D projected trajectories of the NLC droplets ($N = 7$, $D_0 = 19.2 \sim 19.6$ μm) in the same experimental condition as those in the case of the CLC droplets. As previously reported[15,16], we observed deformation of the radial director field of the NLC droplet due to the Marangoni flow inside the droplet. The point defect in the droplet, which is located at the center of the droplet in equilibrium, changed its position toward the direction of the translational motion of the droplet as shown in Fig. 7(b)(c) and

View Article Online
DOI: 10.1039/C7SM00337D

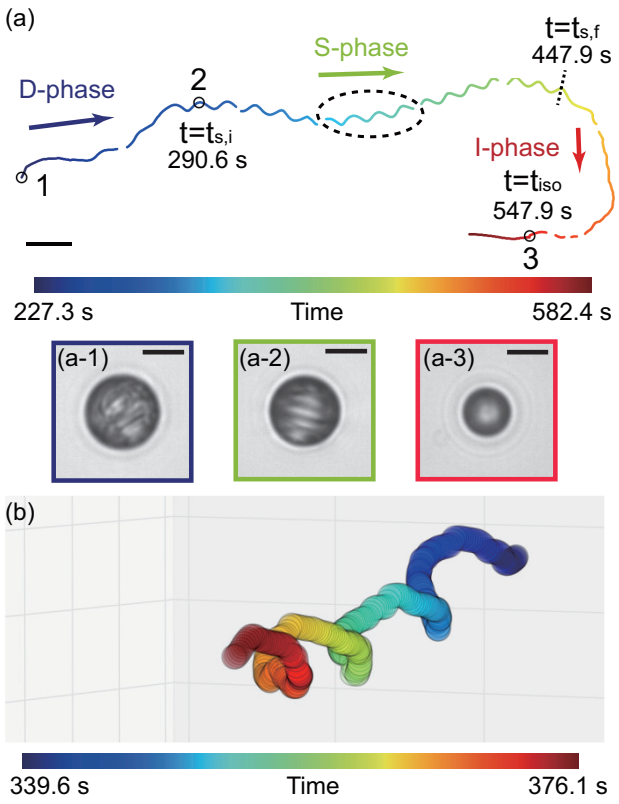

Fig. 6 (a) 2D trajectory of a S811-doped CLC droplet. The textures of the droplets observed at the three points marked with circles in (a) are shown in (a-1)-(a-3), respectively. (b) The 3D trajectory in the region indicated by a dashed ellipse in (a) is shown. The scale bars in (a) and (a-1)-(a-3) are 200 μm and 10 μm, respectively.

(d).

According to these results on R811- and S811-doped CLC droplets and NLC droplets, we conclude that the helical motions of the CLC droplets are induced by the chirality of CLC. Note that Krüger *et al.* recently reported that the helical motions of the NLC droplets appear when the diameter was ~ 50 μm much larger than that of our droplets[16]. In their report, the left- and right-handed helices appear with equal probability because the NLC is achiral. Thus, we find that the NLC droplets show qualitatively different behaviors depending on the droplet size. The mechanism of the emergence of such property of the NLC droplets should be investigated in detail, but is beyond the scope of this paper.

4 Discussion

In Fig. 8, we depict the mechanism of the helical self-propulsion in the S-phase. In the case of the self-propelled NLC droplet, the Marangoni flow in the translational direction occurs inside the droplet as shown in Fig. 7 and previous reports[15,16]. Thus, the Marangoni flow should occur also in the CLC droplet and determine the direction of the self-propelled motion. We consider that the helical motion can be driven by the chiral coupling between the Marangoni flow and the rotational motion through the helical director field of the CLC droplet. Such chiral coupling is proba-

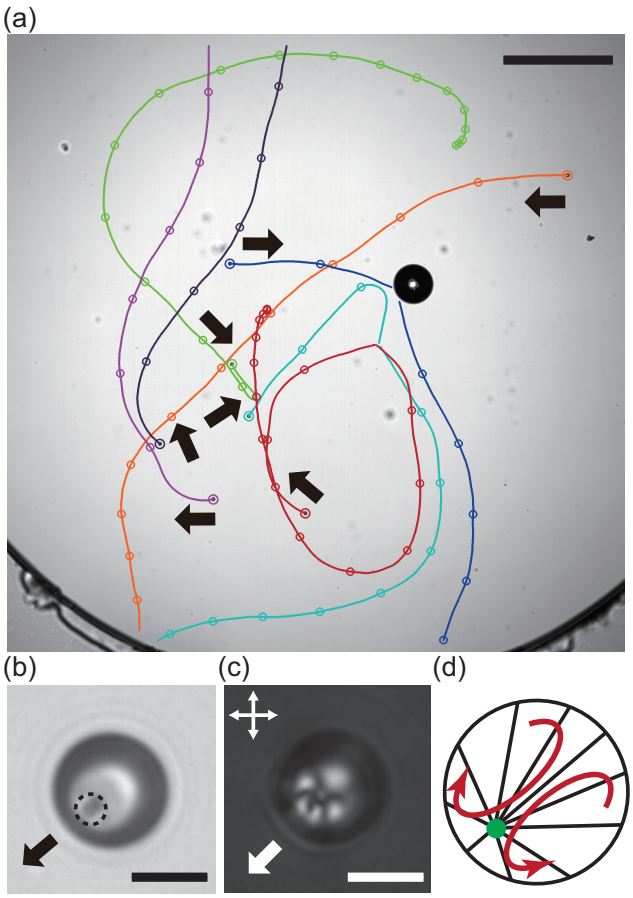

Fig. 7 (a) 2D projected trajectories of the NLC droplets ($N = 7$, injected within 20 s) observed through the low power of microscope ($\times 4$). We drew the trajectories 3 min after the first droplet was injected. The droplets swam in the direction of arrows. The circles on the trajectories were drawn every 30 s. (b)(c) Texture of a NLC droplet during the ballistic swimming observed without and with polarizers (objective, $\times 20$). The arrows represent the direction of motion. The dashed circle in (b) indicates the position of the point defect inside the droplet. Double-headed arrows in (c) indicate the direction of 2 crossed polarizers. The images in (b) and (c) were captured in a larger chamber, since the NLC droplets likely escape outside the view due to the highly ballistic motion. (d) A schematic cross-sectional image of the director field inside the NLC droplet. The direction of the director field and the point defect are drawn as lines and a point, respectively. The red curved arrows represent the Marangoni flow. The scale bars are 500 μm in (a) and 10 μm in (b)(c), respectively.

View Article Online
DOI: 10.1039/C7SM00337D

bly relevant to the Lehmann effect, which is the cross coupling between rotational motion of the CLC and external thermodynamic force[17–20]. We consider that the helical motion appeared only in the S-phase, since the chiral coupling was enhanced due to the highly-ordered structure of the homogeneous helical director field. As a future work for understanding the origin of the chiral coupling, it will be interesting to investigate the effect of handedness of helical director fields (R811: Right-handed and S811: Left-handed[27]) on that of the helical motions (R811: Left-handed and S811: Right-handed) possibly by performing experiments with different LC materials.

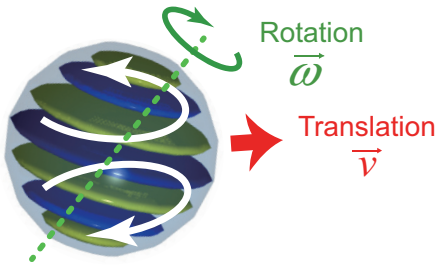

Fig. 8 Schematic image of the mechanism of helical self-propulsion. The white curved arrows in the CLC droplet and red arrow represent the Marangoni flow and the translational motion, respectively. The green dotted line and curved arrow represent the rotational axis and the rotation, respectively.

To summarize, we have experimentally reported the chirality-induced helical motion of the self-propelled CLC droplets. Generally, helical motion appears only when the direction of velocity vector $\vec{v}$ and rotation vector $\vec{\omega}$ of a CLC droplet are neither parallel nor perpendicular. To elucidate why such condition is satisfied in our experiments, investigations on the hydrodynamics inside/outside the droplet are required, perhaps achievable using fluid flow visualization techniques[18] which do not disturb the director field of CLC.

5 Acknowledgements

We thank H. R. Brand, T. Hiraiwa, K. H. Nagai, T. Ohta and M. Tarama for fruitful discussions, T. Hiraiwa, K. Kawaguchi and K. H. Nagai for carefully reading our manuscript, T. Morita and M. Takinoue for advices on the sample preparation, K. Hirosawa and M. Shibayama for the density measurement, and T. Aida, Y. Itoh, S. Tokunaga and K. Yano for the measurement of isotropic phase transition temperature of CLC. This work is supported by Grant-in-Aid for JSPS Fellows (Grant No. 269814), and JSPS KAKENHI Grant No. 25103004, Fluctuation & Structure.

References

1 B. M. Friedrich and F. Jülicher, *Phys. Rev. Lett.*, 2009, **103**, 068102.
2 J. Elgeti, U. B. Kaupp and G. Gompper, *Biophys. J.*, 2010, **99**, 1018.
3 H. C. Crenshaw, *Bull. Math. Biol.*, 1993, **55**, 197.
4 J. Gray, *J. Exp. Biolo.*, 1955, **32**, 775.
5 J. F. Jikeli, L. Alvarez, B. M. Friedrich, L. G. Wilson, R. Pascal, R. Colin, M. Pichlo, A. Rennhack, C. Brenker and U. B. Kaupp, *Nat. Commun.*, 2015, **6**, 7985.
6 B. Liu, M. Gulino, M. Morse, J. X. Tang, T. R. Powers and K. S. Breuer, *Proc. Natl. Acad. Sci. USA*, 2014, **111**, 11252.
7 R. Dreyfus, J. Baudry, M. L. Roper, M. Fermigier, H. A. Stone and J. Bibette, *Nature*, 2005, **437**, 862.
8 C. C. Maass, C. Krüger, S. Herminghaus and C. Bahr, *Ann. Rev. Condens. Matter Phys.*, 2016, **7**, 171.
9 F. Kümmel, B. ten Hagen, R. Wittkowski, I. Buttinoni, R. Eichhorn, G. Volpe, H. Löwen and C. Bechinger, *Phys. Rev. Lett.*, 2013, **110**, 198302.
10 K. Nagai, Y. Sumino, H. Kitahata and K. Yoshikawa, *Phys. Rev. E*, 2005, **71**, 065301(R).
11 Z. Izri, M. N. van der Linden, S. Michelin and O. Dauchot, *Phys. Rev. Lett.*, 2014, **113**, 248302.
12 S. Michelin, E. Lauga and D. Bartolo, *Phys. Fluids*, 2013, **25**, 061701.
13 V. Pimienta, M. Brost, N. Kovalchuk, S. Bresch and O. Steinbock, *Angew. Chem. Int. Ed.*, 2011, **50**, 10728.
14 M. Schmitt and H. Stark, *Phys. Fluids*, 2016, **28**, 012106.
15 S. Herminghaus, C. C. Maass, C. Krüger, S. Thutupalli, L. Goehring and C. Bahr, *Soft Matter*, 2014, **10**, 7008.
16 C. Krüger, G. Klös, C. Bahr and C. C. Maass, *Phys. Rev. Lett.*, 2016, **117**, 048003.
17 O. Lehmann, *Ann. Phys.*, 1900, **2**, 649.
18 J. Yoshioka, F. Ito, Y. Suzuki, H. Takahashi, H. Takizawa and Y. Tabe, *Soft Matter*, 2014, **10**, 5869.
19 P. Oswald and A. Dequidt, *Phys. Rev. Lett.*, 2008, **100**, 217802.
20 T. Yamamoto, M. Kuroda and M. Sano, *Europhys. Lett.*, 2015, **109**, 46001.
21 S. R. de Groot and P. Mazur, *Non-equilibrium Thermodynamics*, Dover publications, Inc., New York, 1984.
22 D. Seč, S. Čopar and S. Žumer, *Nat. Commun.*, 2014, **5**, 3057.
23 T. Orlova, S. J. Aßhoff, T. Yamaguchi, N. Katsonis and E. Brasselet, *Nat. Commun.*, 2015, **6**, 7603.
24 A. G. Chmielewski, *Mol. Cryst. Liq. Cryst.*, 1986, **132**, 339.
25 E. Nowinowski-Kruszelnicki, J. Kędzierski, Z. Raszewski, L. Jaroszewicz, M. Kojdecki, W. Piecek, P. Perkowski, M. Olifierczuk, E. Miszczyk, K. Ogrodnik and P. Morawiak, *Opto-Electron. Rev.*, 2012, **20**, 255.
26 J. R. Blake, *J. Fluid Mech.*, 1971, **46**, 199.
27 I. Gvozdovskyy and L. Lisetski, *Mol. Cryst. Liq. Cryst.*, 2007, **475**, 113.